



# CHORUS

This is the accepted manuscript made available via CHORUS. The article has been published as:

## Experimental and theoretical study of the $6d_{\{3/2\}}$ polarizability of cesium

A. Kortyna, C. Tinsman, J. Grab, M. S. Safronova, and U. I. Safronova

Phys. Rev. A **83**, 042511 — Published 20 April 2011

DOI: [10.1103/PhysRevA.83.042511](https://doi.org/10.1103/PhysRevA.83.042511)

# Experimental and theoretical study of the $6d_{3/2}$ polarizability of cesium

A. Kortyna, C. Tinsman, and J. Grab\*

*Department of Physics, Lafayette College, Easton, Pennsylvania 18042 U.S.A.*

M. S. Safronova

*Department of Physics and Astronomy, 217 Sharp Lab,  
University of Delaware, Newark, Delaware 19716 U.S.A.*

U. I. Safronova

*Physics Department, University of Nevada, Reno,  
Nevada 89557 U.S.A. and Institute of Spectroscopy,  
Russian Academy of Science, Troitsk, Moscow, Russia*

We report the first polarizability measurements of atomic cesium's  $6d_{3/2}$  state. The scalar and tensor polarizabilities are determined from hyperfine-resolved Stark-shift measurements using two-photon laser-induced-fluorescence spectroscopy of an effusive beam. The resulting values are  $\alpha_0 = -5310(180)a_0^3$  and  $\alpha_2 = 8650(260)a_0^3$ . In addition, our measurements yield the hyperfine coupling constants  $A = 16.36(15)\text{MHz}$  and  $B = -0.7(8)\text{MHz}$ , which agree with previous measurements. We also present relativistic all-order calculation of both scalar and tensor polarizabilities. The resulting theoretical values,  $\alpha_0 = -5686(121)a_0^3$  and  $\alpha_2 = 8750(82)a_0^3$ , are in agreement with the present experimental results.

## I. INTRODUCTION

Accurate knowledge of atomic polarizabilities is important for a variety of applications including: the development of the next-generation atomic time and frequency standards, optical cooling and trapping schemes, the study of fundamental symmetries, thermometry and other macroscopic standards, quantum information with neutral atoms, the study of cold degenerate gases and long-range interactions, atomic transition rate determinations, and benchmark comparisons of theory and experiment [1].

For example, an imperfect knowledge of atomic polarizabilities presents a problem in accurate determination of blackbody radiation (BBR) shifts. At the present time, BBR shifts are the largest source of uncertainty for most new-generation optical frequency standards [2]. Polarizabilities have also been used to determine specific electric-dipole matrix elements needed for other applications [3].

Accurate atomic-structure calculations are critical for interpreting studies of parity-nonconserving (PNC) interactions with heavy atoms. To date, the most accurate atomic-physics PNC measurement has been carried out in atomic cesium [4]. Interpreting these measurements requires the accurate calculation of the tensor transition polarizability and the parity-violating amplitude. Understanding the reliability of these calculations is needed to effectively analyze experimental PNC results [5].

Accurate polarizabilities for group I and II atoms and ions of the periodic table have recently become available

through a variety of techniques. However, most of the experimental and theoretical studies have focused on the ground and lowest excited states. As demonstrated by the recent review [1], few of the the excited-state polarizabilities are known accurately even for the alkali-metal atoms. Cesium is an exception, as it has been the subject of a larger number of such studies owing to its importance for PNC investigations.

Although the polarizabilities for a wide range of atomic cesium states have been reported to date, many of the values represent data that are decades old and of low precision. Table X in Mitroy et al. [1] provides an overview of the many experimentally and theoretically determined polarizabilities of cesium. Among these, examples of notable measurements include very high precision results for the  $6s_{1/2}$  [6], the  $6p_{1/2}$  [7], and the  $6p_{3/2}$  [8, 9] states. The polarizabilities of essentially all the lower-lying states of cesium have also been calculated. These calculation were carried out using using both the Coulomb approximation [10] and a relativistic all-order method [11, 12].

From Ref. [1], we see that experimental results exist for most of the lowest-lying states of cesium with the notable exceptions of the  $5d_j$  and  $6d_j$  states. In the present article, we report the first measurements of the scalar and tensor polarizabilities of cesium's  $6d_{3/2}$  state using hyperfine-resolved, two-photon fluorescence spectroscopy of an effusive beam with single-mode tunable lasers. As a test of the high-precision methodology, we also carry out calculations of both the scalar and tensor polarizabilities for this state. We note that these quantities are particularly suitable for such a test owing to significant cancellations of various contributions.

The study of the  $nd$  state polarizabilities in monovalent systems is also important for the development of optical frequency standards with  $\text{Ca}^+$  and  $\text{Sr}^+$  ions. In

---

\*Department of Physics, Cornell University, 109 Clark Hall, Ithaca, NY 14853-2501 U.S.A.

both of these cases,  $nd_{5/2}$  states are used as upper clock levels, so their polarizabilities must be precisely known for evaluating the BBR shift [13, 14].

In this work, we have also determined the  $6d_{3/2}$  hyperfine coupling constants. By comparing these hyperfine measurements to literature values we gain confidence that our frequency scale is well calibrated.

Below, we discuss the experimental determination of the polarizabilities and hyperfine constants in Sec. II. Theoretical calculations of the scalar and tensor polarizabilities are discussed in Sec. III. The comparison of the experimental and theoretical values is discussed in Sec. IV.

## II. EXPERIMENT

To maintain the hyperfine-resolved nature of our measurements, we choose a range of electric fields over which the Stark shift is comparable in magnitude to the hyperfine splitting. This preserves the magnetic sub-levels as members of the total angular momentum manifolds and permits the application of perturbation theory to the combined hyperfine-Stark perturbation. As outlined in Ref. [15], the perturbation Hamiltonian is the sum of the hyperfine interaction operator,  $V_{hf}$ , and the Stark interaction operator,  $V_S$ ,

$$H = V_{hf} + V_S. \quad (1)$$

The hyperfine operator is diagonal in  $F$  and  $m$ , the total atomic angular momentum and its projection onto the quantization axis. The first two terms of these matrix elements are given by

$$\langle Fm|V_{hf}|Fm\rangle = \frac{1}{2}AK + \frac{1}{4}B\frac{\frac{3}{2}K(K+1) - 2I(I+1)J(J-1)}{I(2I-1)J(2J-1)} \quad (2)$$

where  $A$  is the magnetic dipole coupling constant,  $B$  is the electric quadrupole coupling constant,  $J$  is the

electronic angular momentum,  $I$  is the nuclear angular momentum, and  $K = F(F+1) - J(J+1) - I(I+1)$ .

For nondegenerate states, the first-order Stark interaction is zero. This results in the Stark term being quadratic in the electric field,  $\epsilon$ . The Stark interaction matrix element is diagonal in  $m$  and is typically written as the sum of two terms

$$\langle Fm|V_S|F''m\rangle = -\frac{1}{2}\alpha_0\epsilon^2\delta_{F,F''} - \frac{1}{2}\alpha_2\epsilon^2\langle Fm|Q|F''m\rangle, \quad (3)$$

where  $\alpha_0$  is the scalar polarizability,  $\alpha_2$  is the tensor polarizability,  $\delta_{F,F''}$  is the Kronecker delta, and  $Q$  is the operator describing the Stark mixing of the hyperfine levels.

The combined hyperfine-Stark interaction is evaluated by diagonalizing the explicit perturbation Hamiltonian

$$V_{F,F'';m} = \langle Fm|V_{hf}(F = F'')|F''m\rangle + \langle Fm|V_S|F''m\rangle. \quad (4)$$

The hyperfine term can be either deduced from Eq. (2) or determined experimentally (which is the method used here). The individual matrix elements of the Stark term can be computed using  $3 - j$  and  $6 - j$  symbols (for example, see Ref. [16]).

Because the Stark interaction is diagonal in  $m$ , diagonalizing Eq. (4) can be simplified by a judicious choice of the specific  $|Fm\rangle$  levels used in the polarizability analysis. Figure 1 shows a schematic of the relevant hyperfine manifolds involved in this measurement. The  $|Fm\rangle = |5, 5\rangle$  sub-level of the  $6d^2D_{3/2}$  state cannot mix with any other state, so it is associated with the simplest perturbation Hamiltonian and represented by the  $1 \times 1$  matrix

$$V_{5,F'';5} = -\frac{1}{2}\alpha_0\epsilon^2 - \frac{1}{2}\alpha_2\epsilon^2 + \langle 5, 5|V_{hf}|5, 5\rangle. \quad (5)$$

The  $|Fm\rangle = |5, 4\rangle$  sub-level is the next simplest case because it mixes with only the  $|Fm\rangle = |4, 4\rangle$  sub-level. This yields a  $2 \times 2$  matrix

$$V_{5,F'';4} = -\frac{1}{2}\alpha_0\epsilon^2 - \begin{pmatrix} \frac{1}{5}\alpha_2\epsilon^2 - \langle 5, 4|V_{hf}|5, 4\rangle & \frac{\sqrt{21}}{5}\alpha_2\epsilon^2 \\ \frac{\sqrt{21}}{5}\alpha_2\epsilon^2 & -\frac{1}{5}\alpha_2\epsilon^2 - \langle 5, 4|V_{hf}|5, 4\rangle \end{pmatrix}. \quad (6)$$

The  $|5, 5\rangle$  and  $|5, 4\rangle$  sublevels have the added advantage of being the easiest of the  $6d_{3/2}$  magnetic sublevels in cesium to isolate experimentally.

The scalar polarizability can be determined from Eq. (5) by plotting the Stark shift of the  $|5, 5\rangle$  peak as a function of  $\epsilon^2$ , but first the tensor polarizability must be found. This is done by diagonalizing Eq. (6), and subtracting the  $|5, 4\rangle$  eigenvalue from the  $|5, 5\rangle$  eigenvalue of

Eq. (5). This provides an expression for  $\alpha_2$  in terms of  $h\nu_{54}$ , the splitting between the  $|5, 5\rangle$  and  $|5, 4\rangle$  substates,

$$\frac{10}{3} \frac{\left(1 - \frac{\nu_{54}}{\nu_{hf}}\right) h\nu_{54}}{\left(1 - \frac{10}{3} \frac{\nu_{54}}{\nu_{hf}}\right)} = -\alpha_2\epsilon^2, \quad (7)$$

where  $h\nu_{hf}$  is the hyperfine splitting between the  $F = 5$

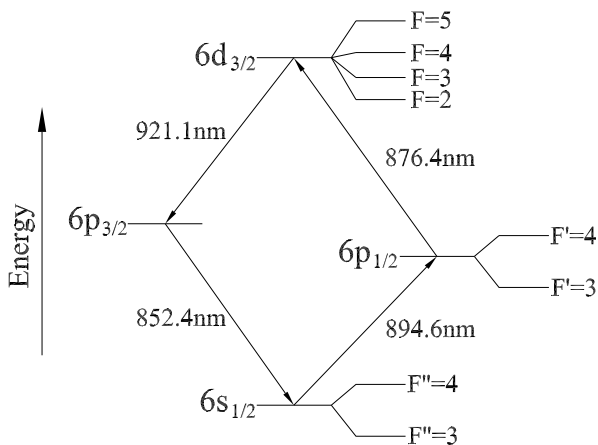


FIG. 1: The relevant hyperfine manifolds. Also illustrated are the laser-excitation and fluorescence-detection schemes of the  $6d_{3/2}$  state of cesium. Two single-mode lasers excite the  $6s_{1/2}(F'' = 4) \rightarrow 6p_{1/2}(F' = 3 \text{ or } 4) \rightarrow 6d_{3/2}(F)$  resonant two-photon transition. Absorption of the 876.4 nm laser beam is monitored in a vapor cell and 852.4 nm fluorescence is detected from an effusive beam.

and  $F = 4$  states at zero field. The tensor polarizability is thus found by plotting the left side of Eq. (7) against  $\epsilon^2$ .

### A. Apparatus

Figure 2 shows a schematic of the experimental setup. The Stark shifts and the hyperfine intervals of the  $6d_{3/2}$  state of cesium are measured with hyperfine-resolved, resonant two-photon spectroscopy. Two single-mode external-cavity diode lasers probe a well collimated effusive beam using laser-induced-fluorescence (LIF) spectroscopy and simultaneously probe a vapor cell using absorption spectroscopy with phase-sensitive detection. A well characterized electric field splits the hyperfine magnetic sublevels in the effusive beam while the vapor cell is held in a field-free region. Stark shifts are measured in the effusive beam, and the vapor cell provides frequency-scale calibration. The frequency scale is directly referenced to a rubidium frequency standard using an optical modulation technique.

Figure 1 provides an overview of the spectroscopic schemes used for state preparation and signal acquisition. These schemes have been described in detail elsewhere: laser excitation and fluorescence detection from a effusive beam in Ref. [17]; laser excitation and absorption detection from the vapor cell in Ref. [18]. Briefly, the linearly polarized beams from two single-mode, external-cavity diode lasers (DL1 and DL2 in Fig. 2) are split and sent simultaneously through an effusive beam and a vapor cell. The beams from DL1 and DL2 counter-propagate through both the effusive beam and the vapor cell with their polarization vectors aligned.

About 10% of the output from DL1 is directed into a saturated-absorption spectrometer where DL1 is center locked to the  $6s_{1/2}(F'' = 4) \rightarrow 6p_{1/2}(F' = 3 \text{ or } 4)$  transition at  $\lambda_1 \approx 894.6$  nm using a phase-sensitive servo. The second diode laser, DL2, is scanned across the  $6p_{1/2}(F' = 3 \text{ or } 4) \rightarrow 6d_{3/2}(F = 2, \dots, 5)$  manifold at  $\lambda_2 \approx 876.4$  nm. The DL2 cavity length, and thus its wavelength, is varied with a piezo-electric crystal. The potential difference across the piezo-electric crystal is controlled by a 12-bit digital-to-analog converter (DAC). The hyperfine measurements include data from all three  $6d_{3/2}(F = 2, \dots, 5)$  intervals, whereas the polarizability requires measuring only the interval between the  $m = 4$  to  $m = 5$  magnetic sublevels of the  $6d_{3/2}(F = 5)$  manifold.

For LIF detection, the  $6p_{3/2} \rightarrow 6s_{1/2}$  fluorescence signal from the effusive beam is passed by a 852 nm interference filter to a photomultiplier tube (PMT). The DL2 wavelength is stepped across the the  $6p_{1/2} \rightarrow 6d_{3/2}$  hyperfine transitions (by incrementing the DAC setting) and the photon count rate is collected by a counter-timer board and stored in a microcomputer. Simultaneously, the absorption signal from the cesium vapor cell is monitored using phase-sensitive detection.

To implement phase-sensitive detection, the DL1 beam is amplitude modulated at about 17.4 kHz using using a 40MHz acousto-optical modulator (40MHz AOM). The DL2 beam is monitored with a photodiode (PD) and a lockin amplifier (a SRS model SR830 DSP Lockin Amplifier). These data are encoded by a 12-bit analog-to-digital converter (with 2.4 mV resolution) and stored along side the LIF count rate for each DL2 wavelength.

The effusive beam apparatus is contained inside a differentially pumped vacuum chamber. The beam-source chamber pressure is approximately  $5 \times 10^{-6}$  mbar and the fluorescence-detection chamber pressure is approximately  $5 \times 10^{-8}$  mbar. The beam source is held at about 200°C, creating a cesium vapor pressure of about 0.1 mbar. This vapor effuses through a 0.5 mm nozzle. Two apertures collimate the beam to a divergence of 4.2 mrad, and the cesium flux is  $10^{10}$  atoms/sec. At the intersection between the effusive beam and the laser beams, a uniform DC electric field is established between two parallel copper plates. Each plate is 90 mm in diameter and ground to a flatness of  $\pm 0.05$  mm. They are held at a separation of 14.7(2) mm by four insulating posts — the uncertainty in plate separation is our chief contribution to systematic error.

An electric potential of up to 10.6 kV is applied across these plates. This potential difference is monitored with a calibrated precision voltmeter (Keithly model 2000 Multimeter) and a 1000:1 precision voltage divider (Cadock Electronics model HVD Ultra-Precision Voltage Divider). The multimeter has a certified accuracy of eight parts in  $10^5$ , and we have determined the precision of the voltage divider to be better than one part in  $10^3$ .

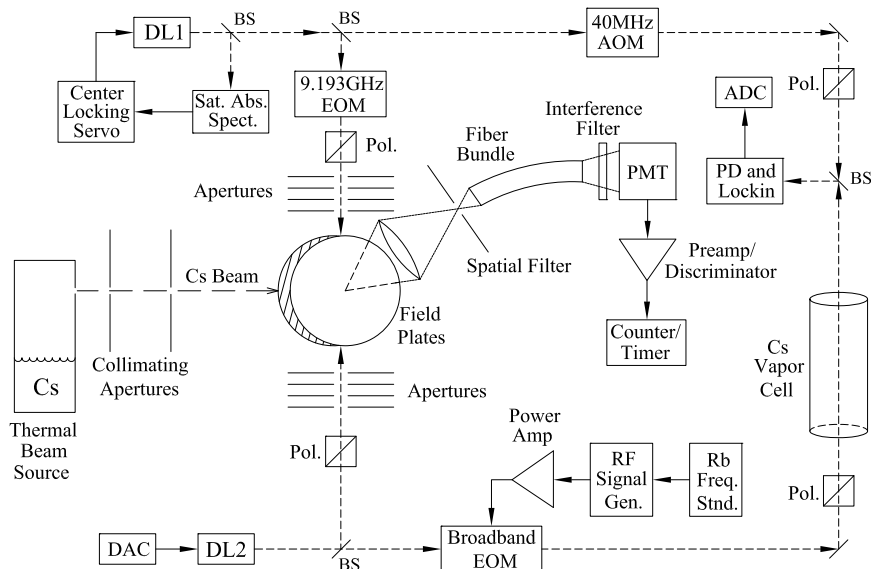


FIG. 2: Apparatus for measuring Stark shifts and hyperfine intervals of the  $6d_{3/2}$  state of cesium. Symbols in the diagram have the following meanings — 9.193GHz EOM: 9.193GHz electro-optical modulator; 40MHz AOM: 40MHz acousto-optical modulator; ADC: 12-bit analog-to-digital converter; Broadband EOM: 1-250MHz electro-optical modulator; BS: beam splitter; DAC: 12-bit digital-to-analog converter; DL1 and DL2: single-mode external-cavity diode lasers; PD and Lockin: photodiode and phase-sensitive lockin amplifier; PMT: photomultiplier tube; Pol.: high contrast linear polarizer; Rb Freq. Std.: 10MHz rubidium frequency standard; RF Signal Gen.: 1kHz-2GHz radio-frequency signal generator; Sat. Abs. Spect.: saturated-absorption spectrometer; solid lines: signal paths; short dashed line: laser beam paths; long dashed lines: cesium beam path.

### B. Frequency calibration

We calibrate the laser frequency scale using a modification of the technique described in Ref. [18]. The scanned laser beam (from DL2) is split and simultaneously passes through the effusive beam and the absorption cell. Prior to passing into the absorption cell, a broadband electro-optical modulator (EOM) adds modulation sidebands to the DL2 frequency. In this experiment, we choose among three modulation frequencies: 115 MHz for the Stark shift measurements, and either 155 MHz or 210 MHz for the hyperfine splitting measurements (155 MHz for the  $6p_{1/2}(F' = 3) \rightarrow 6d_{3/2}(F = 2, 3, 4)$  transitions and 210 MHz for the  $6p_{1/2}(F' = 4) \rightarrow 6d_{3/2}(F = 3, 4, 5)$  transitions). These values are chosen to optimize modulation efficiency and to match the intervals being measured without obscuring spectral features. The modulation frequencies are directly referenced to a  $^{87}\text{Rb}$  frequency standard. This frequency standard provides both short-term stability and long-term accuracy to better than 5 parts in  $10^9$ .

The broadband EOM produces a dominant sideband on either side of the laser's central frequency. As the laser is scanned across a spectral peak, three features are observed precisely separated by the modulation frequency. The frequency scale for the hyperfine splitting measurements is calibrated using the method of Ref. [17]. For the Stark shift measurements, the relative frequency scale is calibrated by fitting a second-order polynomial to a total of six peaks: the  $6p_{1/2}(F' = 4) \rightarrow 6d_{3/2}(F = 4)$  peak,

the  $6p_{1/2}(F' = 4) \rightarrow 6d_{3/2}(F = 5)$  peak, and the four associated modulation sidebands. The nonlinearity given by these fits is always about 1 part in  $10^4$ .

When we fit a third-order polynomial to the same six points, we find the third-order term to be about two parts in  $10^8$ . We incorporate the uncertainty associated with the third-order term into our systematic error budget (see Sec. II C 2), although this effect does not contribute significantly to the overall uncertainty.

The residual magnetic field can introduce systematic errors into frequency measurements. For example, the optical pumping of differentially shifted magnetic sublevels can cause line centers to shift in frequency. This phenomenon has the potential to introduce nonlinearities into our frequency scale because power density differences between the central laser frequency and the modulation sidebands can produce differential degrees of optical pumping of Zeeman-shifted magnetic sublevels. We employ several measures to minimize the effect of residual magnetic fields. We linearly polarize all laser beams with extinction ratios better than 2000:1. Linearly polarized light limits the dipole-transition selection rules to  $\Delta m = 0$ ; sublevels with the same magnetic quantum number tend to have similar Zeeman shifts. We also use high-permeability shielding in the region where the laser beams intersect the effusive beam. This reduces the residual magnetic field by about one order of magnitude. Since we do not observe significant nonlinearity of our frequency scale, we conclude that our frequency calibration technique is not sensitive to optical pumping effects.

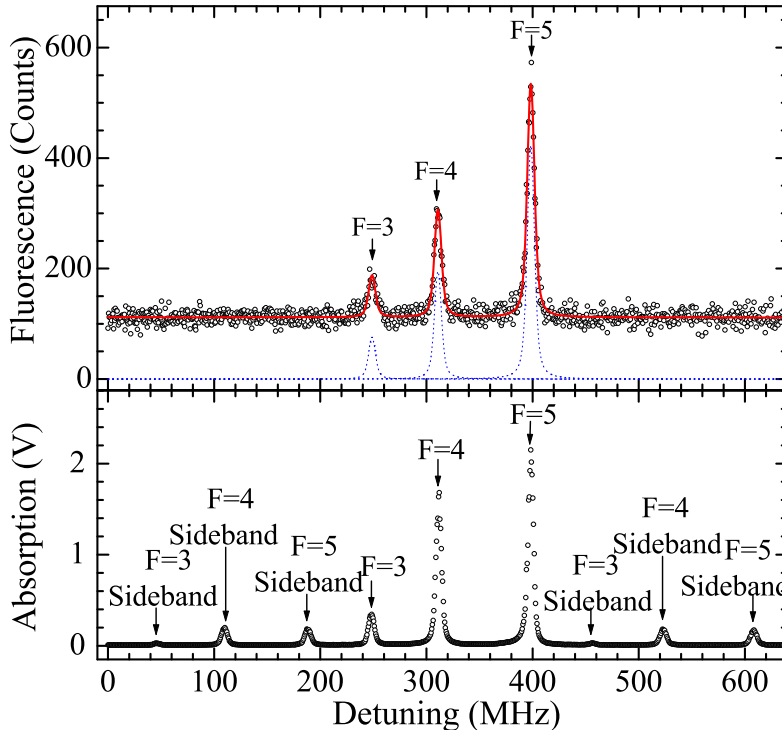


FIG. 3: Two-photon spectra of the  $6d_{3/2}$  ( $F = 3, 4, 5$ ) hyperfine states at zero field. The upper plot shows the laser-induced-fluorescence signal from the effusive beam (circles) with the hyperfine sublevels marked. Also shown are fitted Voigt profiles, offset for clarity (blue dotted line), and the aggregate fit (red solid line). The lower plot shows the frequency-calibration spectrum: the absorption signal from the cesium vapor cell collected concurrent with the upper plot. For the calibration spectrum, the laser is phase modulated at 210 MHz and the locations of the hyperfine sublevels and sidebands are marked. The least-squares fit of Voigt profiles to the lower plot has been omitted for clarity sake.

TABLE I: The magnetic dipole  $A$  and electric quadrupole  $B$  hyperfine coupling constants of cesium's  $6d_{3/2}$  state.

Source	A [MHz]	B [MHz]
Present work	16.36(15)	-0.7(8)
Reference [18]	16.34(3)	-0.1(2)
Reference [19]	16.30(15)	$< \pm 8$
Reference [12]	17.8	

To reduce both optical pumping and power broadening effects, we operate all laser beams at low power densities. In general, we observed line broadening at power densities above  $4 \text{ mW/cm}^2$ . The DL1 laser beam operates between  $0.4 \text{ mW/cm}^2$  and  $1.0 \text{ mW/cm}^2$  and the DL2 laser beam operates between  $0.7 \text{ mW/cm}^2$  and  $1.5 \text{ mW/cm}^2$ . All data presented here are collected at the lower end of these power-density ranges. Collisional broadening and collisional line shifts are not an issue because of the low background pressures in both the fluorescence detection chamber and the absorption cell.

### C. Experimental Results and Data Analysis

Data analysis is divided into two parts. In Sec. II C 1, we verify the accuracy of our frequency scale by generating the hyperfine coupling constants for the  $6d_{3/2}$  state at zero field. In Sec. II C 2, we determine the scalar and tensor polarizabilities of the  $6d_{3/2}$  state.

#### 1. Hyperfine Coupling Constants

Figure 3 shows a typical spectrum of the  $6s_{1/2}(F'' = 4) \rightarrow 6p_{1/2}(F' = 4) \rightarrow 6d_{3/2}(F = 3, 4, 5)$  two-photon transitions at zero field. The upper plot is the laser-induced-fluorescence signal from the effusive beam. The lower plot is the absorption signal from the vapor cell. The lower plot includes the phase-modulation side bands used to calibrate the frequency scale. In this case, the modulation frequency is 210 MHz. Both spectra are collected simultaneously.

Also shown in the upper panel of Fig. 3 are fitted Voigt profiles. A Voigt profile is fitted to each spectral feature

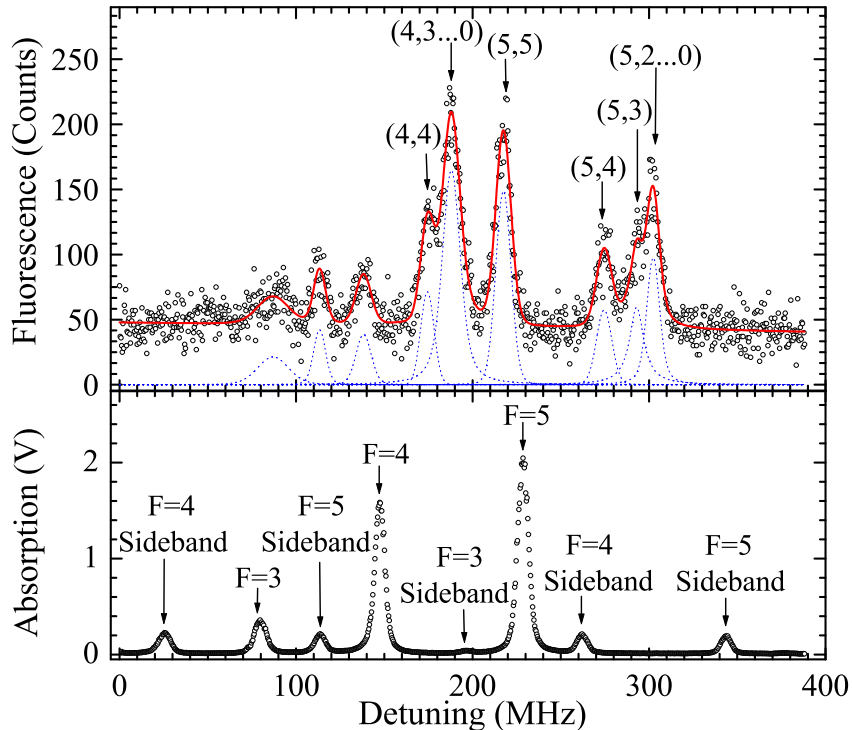


FIG. 4: Stark-shifted two-photon spectra of the  $6d_{3/2}$  ( $F = 3, 4$ , and  $5$ ) hyperfine states. The upper plot is the laser-induced-fluorescence signal from the effusive beam taken at  $6.86(9)$  kV/cm. All  $(F, m)$  sublevels of the  $F = 4$  and  $F = 5$  hyperfine manifold are marked. The  $|5, 5\rangle$  and  $|5, 4\rangle$  states are clearly resolved. Also shown are Voigt profiles fitted to each spectral feature, offset for clarity (blue dotted line), and the aggregate least-squares fit (red solid line). The lower plot shows the frequency-calibration spectrum: the absorption signal from the cesium vapor cell collected concurrent with the upper plot but at zero field. For the calibration spectrum, the scanned laser is phase modulated at 115 MHz and the locations of the hyperfine states and the modulation sidebands are marked. The least-squares fit of Voigt profiles to the lower plot has been omitted for clarity sake.

using a Levenburg-Margquardt residual minimization algorithm. The same nonlinear fitting procedure is applied to the absorption data, although these results are omitted from Fig. 3 for the sake of clarity. Data were collected at 500 kHz intervals, but the fitting procedure allows the centroid of each peak to be determined with an uncertainty of about 100 kHz. The reduced  $\chi^2$  for all fits are on the order of one, and for Fig. 3,  $\chi^2 = 1.1$  for both panels.

We determine the  $F = 4 \rightarrow F = 5$  hyperfine interval to be  $82.46(15)$  MHz by averaging the centroid differences from 50 individual  $6s_{1/2}(F'' = 4) \rightarrow 6p_{1/2}(F' = 4) \rightarrow 6d_{3/2}(F = 3, 4, 5)$  spectra. However, we do not use these spectra to determine the  $F = 3 \rightarrow F = 4$  splitting because of the lower single-to-noise ratio of the  $F = 3$  peak. Instead, we measure the  $F = 2 \rightarrow F = 3$  and the  $F = 3 \rightarrow F = 4$  hyperfine intervals by averaging the centroid differences from 50 individual  $6s_{1/2}(F'' = 4) \rightarrow 6p_{1/2}(F' = 3) \rightarrow 6d_{3/2}(F = 2, 3, 4)$  spectra. These intervals are  $64.71(15)$  MHz and  $49.31(20)$  MHz, respectively.

The hyperfine coupling constants are generated by ap-

plying Eq. (2) to our hyperfine intervals using the method outlined in Ref. [18]. These results are reported in Table I along with equivalent values from the literature. One might expect our results to differ from the literature because of our efforts to minimize magnetic fields and optical pumping effects which had not been done in previous studies. However, our measurements agree closely with those using two-photon absorption spectroscopy in a vapor cell [18], and cascade-radio-frequency spectroscopy [19]. The theoretical relativistic all-order value [12] differ from experiment by 9%. This is not unexpected because correlation correction contributes over 40% for  $A$  with large contributions coming from fourth and higher-orders making accurate modeling of electron-correlation effects very difficult in this case. This issue was discussed in detail in Ref. [12]. Much higher accuracy is expected for the theoretical all-order calculation of polarizabilities.

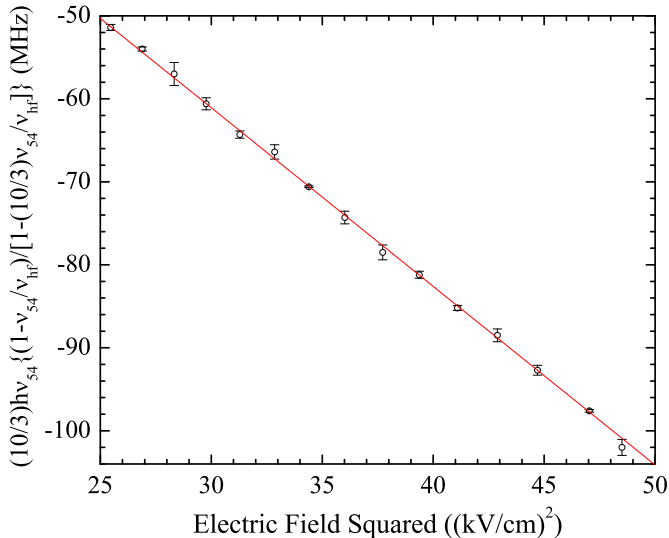


FIG. 5: Equation 7 plotted using our data for the  $|5, 5\rangle$  to  $|5, 4\rangle$  Stark splitting and the  $F = 5$  to  $F = 4$  hyperfine splitting for the  $6d_{3/2}$  state. A linear least-squares fit gives a slope of  $-2.152(11)$  Mhz/(kV/cm) $^2$  or  $-8648(44)$   $a_0^3$ .

## 2. Polarizabilities

Figure 4 shows a typical spectrum of the  $6s_{1/2}(F'' = 4) \rightarrow 6p_{1/2}(F' = 4) \rightarrow 6d_{3/2}(F = 3, 4, 5)$  two-photon transitions at 6.86(9) kV/cm along with the associated frequency-calibration spectrum at zero field. The upper plot is the Stark-shifted laser-induced-fluorescence signal from the effusive beam. The various  $|F, m\rangle$  sublevels are labeled for the  $F = 4$  and  $F = 5$  hyperfine states. The positions of the  $|5, 5\rangle$  and  $|5, 4\rangle$  peaks are needed for our analysis and they are clearly resolved here. We vary the electric field between 5.05(7) kV/cm and 6.96(9) kV/cm and clearly resolve the  $|5, 5\rangle$  and  $|5, 4\rangle$  peaks at every field strength. The lower plot of Fig. 4 shows the frequency-calibration absorption spectrum from the vapor cell at zero field and with 115 MHz phase-modulation applied to the scanned laser. The hyperfine states are labeled along with the modulation sidebands.

The centroid of each spectral feature is determined by fitting Voigt profiles, as described in Sec. II C 1. The  $\chi^2$  values of these fits are on the order of unity. The frequency scale is calibrated by fitting a second-order polynomial to the centroids of the absorption spectrum as described in Sec. II B.

The slight overlap between the  $|5, 4\rangle$  and  $|5, 3\rangle$  peaks caused some concern that the fitting routine might pull the  $|5, 4\rangle$  centroid towards (or away from) the correct  $|5, 4\rangle$  peak position. To estimate the effect of peak overlap, we used our fitting routine to analyze a series of model spectra. To construct a model spectrum, we

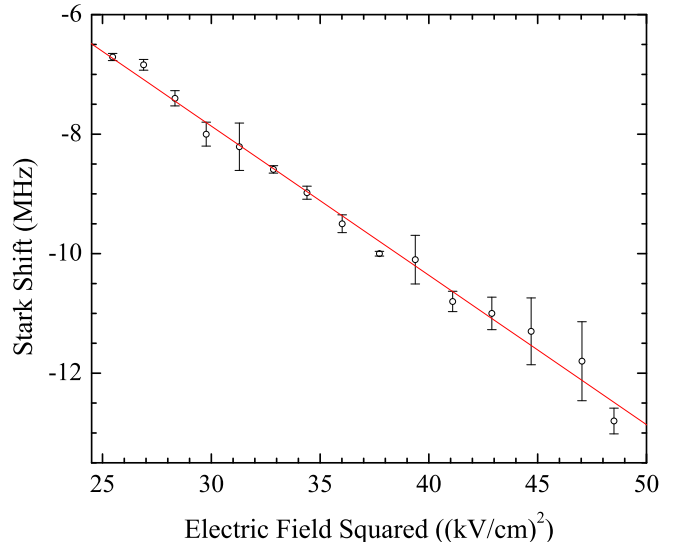


FIG. 6: The net Stark shift of the of the  $|5, 5\rangle$  sublevel of the  $6d_{3/2}$  state. A linear least-squares fit gives a slope of  $-0.2499(68)$  Mhz/(kV/cm) $^2$  or  $-1004(27)$   $a_0^3$ .

placed two Voigt functions with widths and overlaps similar to what we observe experimentally, and add Gaussian noise at levels that mimic the experimental signal-to-noise levels. We then apply our fitting routine to each model spectrum to find the peak centroids. Comparing the fit centroids to the original peak centers shows that the variations in peak positions are small compared to the uncertainty in the fitted centroid. We therefore conclude that the peak overlap does not significantly influence our results.

The scalar and tensor polarizabilities are deduced from data in a two-step procedure. First, the tensor polarizability is found using Eq. (7) by measuring the  $|5, 5\rangle$  to  $|5, 4\rangle$  splitting as a function of the electric field. Second, the scalar polarizability is found using Eq. (5) by measuring the net shift of the  $|5, 5\rangle$  peak as a function of the electric field.

For the tensor polarizability, the  $|5, 5\rangle$  to  $|5, 4\rangle$  splitting provides  $\nu_{54}$  for Eq. (7). The value for  $\nu_{hf}$  is determined in Sec. II C 1. Graphing the left-hand side of Eq. (7) against of  $\epsilon^2$  produces a linear plot with a slope of  $-\alpha_2$ . Using our data, this plot is shown in Fig. 5. A least-squares linear fit yields  $\alpha_2 = 2.152 \pm 0.011 \pm 0.060$  Mhz/(kV/cm) $^2$  or  $8648 \pm 44 \pm 240$   $a_0^3$ , where the first uncertainty is statistical and the second is due to the systematics.

To find  $\alpha_0$ , the net Stark shift of the  $|5, 5\rangle$  sublevel is determined by measuring the interval between the shifted  $|5, 5\rangle$  peak in the effusive beam (for example, the upper plot in Fig. 4) and the simultaneously measured  $F = 5$  peak at zero field in the vapor cell (for example, the lower

TABLE II: Systematic uncertainty budget for the polarizability measurements. Uncertainties are given as relative values.

Reference frequency ( $\delta\nu/\nu$ ):	$2 \times 10^{-10}$
Hyperfine measurement ( $\delta\nu_{hf}/\nu_{hf}$ ):	0.002
Plate separation ( $2\delta d/d$ ):	0.027
Potential difference ( $2\delta V/V$ ):	0.0015
Third-order fit ( $\delta\nu_3/\nu_3$ ):	0.00050
Total:	0.028

plot in Fig. 4) as a function of electric field strength. Applying Eq. 5, the net Stark shift of the  $|5, 5\rangle$  peak,  $h\nu_s$ , is

$$h\nu_s = -\frac{1}{2} [\alpha_0(6d_{3/2}) + \alpha_2(6d_{3/2}) - \alpha_0(6p_{1/2})] \epsilon^2, \quad (8)$$

where  $\alpha_0(6d_{3/2})$  is the scalar polarizability of the  $6d_{3/2}$  state,  $\alpha_2(6d_{3/2})$  is the tensor polarizability of the  $6d_{3/2}$  state, and  $\alpha_0(6p_{1/2})$  is the scalar polarizability of the  $6p_{1/2}$  state.

Figure 6 shows  $h\nu_s$  as a function of  $\epsilon^2$ . A linear fit gives a slope of  $-0.2499(68)$  MHz/(kV/cm)<sup>2</sup> or  $-1004(27)$  a<sub>0</sub><sup>3</sup>. To evaluate  $\alpha_0(6d_{3/2})$ , we use the value  $\alpha_0(6p_{1/2}) - \alpha_0(6s_{1/2}) = 927.35(0.12)$  a<sub>0</sub><sup>3</sup> [7] and  $\alpha_0(6s_{1/2}) = 401.0 \pm 0.6$  a<sub>0</sub><sup>3</sup> [6], where  $\alpha_0(6s_{1/2})$  is the scalar polarizability of the  $6s_{1/2}$  state. This yields a scalar polarizability  $\alpha_0(6d_{3/2}) = -5309 \pm 69 \pm 150$  a<sub>0</sub><sup>3</sup>. Again, the first uncertainty is statistical and the second is due to the systematics.

Table II gives an accounting of our systematic error budget. The reference frequency uncertainty,  $\delta\nu/\nu$ , arises from the long-term drift of the 10 MHz rubidium frequency standard due to aging. The hyperfine uncertainty,  $\delta\nu_{hf}/\nu_{hf}$ , is the statistical uncertainty of our hyperfine measurement. The plate separation uncertainty,  $2\delta d/d$ , is derived from physical measurements of the field plates — this contribution dominates our overall uncertainty. The potential difference uncertainty,  $2\delta V/V$ , is the combined accuracy of the voltmeter and the voltage divider. The third-order fitting uncertainty,  $\delta\nu_3/\nu_3$ , is found by examining the magnitude of the third-order coefficient of the frequency scale fitting function. In practice, only second-order fitting functions are used for data analysis.

### III. THEORETICAL DETERMINATION OF SCALAR AND TENSOR $6d_{3/2}$ POLARIZABILITIES

The scalar,  $\alpha_0$ , and tensor,  $\alpha_2$ , polarizabilities of Cs in an excited state  $v$  are given by [1]

$$\alpha_0 = \alpha_{\text{core}} + \frac{2}{3(2j_v + 1)} \sum_{nlj} \frac{|\langle v || d || nlj \rangle|^2}{E_{nlj} - E_v}, \quad (9)$$

$$\alpha_2 = (-1)^{j_v} \sqrt{\frac{40j_v(2j_v - 1)}{3(j_v + 1)(2j_v + 1)(2j_v + 3)}} \times \sum_{nlj} (-1)^j \begin{Bmatrix} j_v & 1 & j \\ 1 & j_v & 2 \end{Bmatrix} \frac{|\langle v || d || nlj \rangle|^2}{E_{nlj} - E_v}, \quad (10)$$

where  $\langle i || d || j \rangle$  is a reduced electric-dipole matrix element and  $n, l, j$  are the principal, electronic angular momentum, and total angular momentum quantum numbers of the excited state. The Cs<sup>+</sup> ionic core polarizability  $\alpha_{\text{core}}$  is small ( $15.8$  a<sub>0</sub><sup>3</sup>) and is taken from coupled-cluster calculation of Ref. [20]. The correction to the ionic core polarizability that accounts for the presence of the respective valence electron is negligible for the  $6d_{3/2}$  state. Evaluation of the remaining terms requires the knowledge of the reduced electric-dipole matrix elements for the  $6d_{3/2} - np_j$  and  $6d_{3/2} - nf_{5/2}$  transitions. Our calculations are carried out with the finite basis set constructed using B-splines [21] making the sums in Eqs. (9) and (10) finite.

We calculate electric-dipole matrix elements up to  $n = 26$  using the all-order (linearized coupled-cluster) method described in review [22] and references therein. Our calculation of the polarizabilities and their uncertainties follows recent work on Ca<sup>+</sup> polarizabilities [13].

In the linearized coupled-cluster formalism, restricting the expression for the all-order wave function of a monovalent atom in state  $v$  to single, double, and valence triple excitations yields the following expansion [22]:

$$|\Psi_v\rangle = \left[ 1 + \sum_{ma} \rho_{ma} a_m^\dagger a_a + \frac{1}{2} \sum_{mnab} \rho_{mnab} a_m^\dagger a_n^\dagger a_b a_a + \sum_{m \neq v} \rho_{mv} a_m^\dagger a_v + \sum_{mna} \rho_{mnva} a_m^\dagger a_n^\dagger a_a a_v + \frac{1}{6} \sum_{mnrab} \rho_{mnrva} a_m^\dagger a_n^\dagger a_r^\dagger a_b a_a a_v \right] |\Psi_v^{(0)}\rangle, \quad (11)$$

where the indices  $m, n$ , and  $r$  range over all possible virtual states while indices  $a$  and  $b$  range over all occupied core states and  $|\Psi_v^{(0)}\rangle$  is the lowest-order Dirac-Fock (DF) atomic state vector.

In order to establish the uncertainty of the matrix elements that give dominant contributions to the  $6d_{3/2}$  polarizability, we carry out separate calculations with and without the triple excitation term given by the last line of Eq. (11). We refer to the results of these two *ab initio* calculations as single-double (SD) and single-double partial triple (SDpT) values, respectively. We also estimate omitted correlation correction terms in both of these approximations using semi-empirical scaling procedure described in detail in [13]. The resulting values are referred to as SD<sub>sc</sub> and SDpT<sub>sc</sub> data in text and tables below. In summary, four calculations in different all-order approximations (SD, SDpT, SD<sub>sc</sub> and SDpT<sub>sc</sub>) were carried out for each of the  $6d_{3/2} - 6p_j$ ,  $6d_{3/2} - 7p_j$ ,

TABLE III: Recommended values of the reduced electric-dipole matrix elements in  $a_0^3$ . The lowest-order DF and all-order SD and SDpT values are listed; the label “sc” indicates the scaled values. Final recommended values and their uncertainties are given in the column labelled “Final”. The last column gives relative uncertainties of the final values in %. Absolute values are given.

Transition	DF	SD	SD <sub>sc</sub>	SDpT	SDpT <sub>sc</sub>	Final	Unc. (%)
$6d_{3/2} - 4f_{5/2}$	25.582	24.399	24.615	24.619	24.522	24.615(92)	0.38%
$6d_{3/2} - 5f_{5/2}$	9.611	3.266	3.957	4.023	3.770	3.96(19)	4.7%
$6d_{3/2} - 6f_{5/2}$	5.237	2.612	2.895	2.969	2.870	2.895(74)	2.5%
$6d_{3/2} - 6p_{1/2}$	2.623	4.343	4.241	4.145	4.193	4.241(97)	2.3%
$6d_{3/2} - 6p_{3/2}$	1.337	2.147	2.092	2.052	2.075	2.092(40)	1.9%
$6d_{3/2} - 7p_{1/2}$	19.619	17.772	17.988	18.035	17.944	17.988(48)	0.27%
$6d_{3/2} - 7p_{3/2}$	8.863	7.969	8.073	8.096	8.053	8.073(23)	0.29%

TABLE IV: Contributions to the  $6d_{3/2}$  scalar ( $\alpha_0$ ) and tensor ( $\alpha_2$ ) polarizabilities of Cs in  $a_0^3$ . Uncertainties are given in parenthesis.

Contribution	$\alpha_0$	$\alpha_2$
$6p_{1/2}$	-58(3)	58(3)
$7p_{1/2}$	-14372(76)	14372(76)
$8p_{1/2}$	294(19)	-294(19)
$9p_{1/2}$	18(1)	-18(1)
$np_{1/2}$	11	-11
$6p_{3/2}$	-15(1)	-12
$7p_{3/2}$	-3711(21)	-2969(17)
$8p_{3/2}$	45(3)	36(3)
$9p_{3/2}$	3	2
$np_{3/2}$	2	2
$4f_{5/2}$	11766(88)	-2353(18)
$5f_{5/2}$	131(12)	-26(2)
$6f_{5/2}$	53(3)	-11(1)
$7f_{5/2}$	25(2)	-5
$8f_{5/2}$	14(1)	-3
$9f_{5/2}$	9(1)	-2
$nf_{5/2}$	85(5)	-17(1)
Core	16	
Total	-5686(121)	8750(82)

$6d_{3/2} - 8p_j$ ,  $6d_{3/2} - 9p_j$ ,  $6d_{3/2} - 4f_{5/2}$ ,  $6d_{3/2} - 5f_{5/2}$ , and  $6d_{3/2} - 6f_{5/2}$  matrix elements to establish uncertainties of these values. The results for the most important transitions are listed in Table III. Absolute values of the reduced matrix elements in atomic units ( $a_0e$ ) are given, where  $a_0$  is the Bohr radius. The lowest-order Dirac-Fock (DF) values are also listed to demonstrate the size of the correlation correction. SD<sub>sc</sub> values are taken as final. The uncertainty of the final values is estimated as a maximum of the difference between the final values and SDpT *ab initio* and scaled results. Strategies to determine uncertainties of the all-order values was discussed in detail in Ref. [13]. The relative uncertainties in percent are listed in the last column of Table III. We find the size of the correlation correction to be a good indicator of the accuracy of the final values. For example, the correlation correction reduces the lowest-order value for the  $6d_{3/2} - 5f_{5/2}$  transition by 60%. Our final value for

this matrix element is accurate to only about 5% since the contributions of the higher-order correlation corrections are very large resulting in discrepancies between all-order calculations in different approximations. However, only three transitions strongly dominate both scalar and tensor polarizabilities:  $6d_{3/2} - 4f_{5/2}$ ,  $6d_{3/2} - 7p_{1/2}$ , and  $6d_{3/2} - 7p_{3/2}$ . In all of these cases, correlation is rather small ranging from 4 to 10%. Therefore, our accuracy for these transitions is expected to be very high. Our estimated uncertainties in these matrix elements range from 0.27% to 0.38%.

We list the contributions to the  $6d_{3/2}$  scalar ( $\alpha_0$ ) and tensor ( $\alpha_2$ ) polarizabilities of Cs in Table IV. All data are given in atomic units,  $a_0^3$ . Uncertainties are given in parenthesis. The larger contributions are listed individually. The rows labeled “ $np_j$ ” and “ $nf_{5/2}$ ” give the remainders of the corresponding sums. For example, row “ $np_{1/2}$ ” lists the sum of all  $np_{1/2}$  contributions with  $n > 9$ . SD<sub>sc</sub> matrix elements and experimental energies [23, 24] are used for  $np_j$  contributions with  $n < 12$  and  $nf_{5/2}$  contributions with  $n < 11$ . SD matrix elements and energies are used for higher- $n$  contributions up to  $n > 26$ . The remaining terms are negligible and are evaluated in the lowest-order DF approximation. The uncertainties in the polarizability contributions are twice those of the corresponding matrix elements according to Eqs. (9) and (10). The uncertainties of the final results are obtained by adding uncertainties of the individual terms in quadrature.

#### IV. COMPARISON OF THE RESULTS

Table V compares the present experimental, present theoretical, and past theoretical polarizability results. Our measurements agree well with Coulomb approximation (CA) calculations [10], however the CA calculations are not expected to be of high precision. The agreement is also good with the more sophisticated relativistic all-order calculations of Refs. [1, 11]. Present theoretical results are in agreement with Refs. [1, 11] but are substantially more accurate. The present experimental and theoretical values for the tensor polarizability are in

TABLE V: Comparison of the theoretical and experimental values for the  $6d_{3/2}$  scalar and tensor polarizabilities in cesium in  $a_0^3$ . The stated experimental uncertainties are quadrature combinations of statistics and systematics.

	$\alpha_0$	$\alpha_2$
Present (Expt.)	-5310(170)	8650(260)
Present (Theory)	-5686(121)	8750(82)
Ref. [10]	-5320	8620
Refs. [1, 11]	-5680(450)	8770(360)

agreement within the experimental precision. The scalar values differ by less than two combined experimental-theoretical standard deviations.

We note significant cancellation of the dominant contributions in the theoretical calculations which is particularly strong for the scalar polarizability. As a result, the final uncertainty in value of the scalar polarizability (2%) is significantly higher than the uncertainties of the individual contributions. As an additional check of the accuracy of our  $\alpha_0$  result, we carry out the calculation of the scalar polarizability using *ab initio* SD matrix elements instead of our final scaled values; experimental energies are still used for consistency. The resulting SD number,  $-5572 a_0^3$ , is within the estimated uncertainty of our final result,  $-5686(121) a_0^3$ . This indicates that the strong cancellation between various terms also leads to partial cancellation of the higher-order correlation contributions. Otherwise, we would have seen much larger differences between final and SD values. We therefore expect the theoretical estimate of the uncertainty to be reliable.

There is the possibility that our experimental results are biased by the optical pumping of magnetic sublevels. We attempt to mitigate such effects by minimizing the residual magnetic field and by using linearly polarized light (see Sec. II B). To test the effect of optical pumping, we varied the laser power densities by a factor of two and saw a statistically significant variations in neither  $\alpha_0$  nor  $\alpha_2$ . (The experimental results quoted in Table V are for measurements at the lowest power densities.) We have also measured the polarizabilities using laser beams with crossed polarization axes rather than parallel polarization axes. This changes the y-intercept in Fig. 6 by 1.7(7) MHz, but neither of the slopes in Figs. 5 and 6 changed. We presume the small shift in the y-intercept is due to a population shift caused by the projection of the magnetic sublevels onto a different bases, but the slopes are (and should be) independent of sublevel populations in our measurements.

The scalar polarizability is also susceptible to small drifts of the locked laser DL1. The broad Doppler width inherent to the vapor cell allows the position of absorption peaks to drift with DL1, but the fluorescence signal from the effusive beam can only drift by the  $\pm 1$  MHz Doppler width of the effusive beam. The tensor polarizability is not susceptible to this drift because the interval being measured is between two fluorescence peaks from the effusive beam; drifts in DL1 will cause the fluorescence signal to decrease but will leave the frequency interval essentially unchanged. To minimize the effect of DL1 drifting on the scalar polarizability, we carefully monitor the locking servo's error signal during data collection to insure that thermal fluxuations do not pull the lock away from the center frequency.

## V. CONCLUSION

We present high-precision calculations for the  $6d_{3/2}$  polarizability of cesium. We also present the first polarizability measurements for this state. Relativistic all-order calculations produce scalar and tensor polarizabilities of  $\alpha_0 = -5686(121) a_0^3$  and  $\alpha_2 = 8750(82) a_0^3$ . These values are in agreement with measurements using hyperfine-resolved two-photon laser-induced fluorescence from an effusive cesium beam. The resulting empirical polarizabilities are  $\alpha_0 = -5310(170) a_0^3$  and  $\alpha_2 = 8650(260) a_0^3$ . Both our theoretical and experimental results agree with previous calculations [1, 10, 11].

The experimental frequency scale is calibrated using the absorption signal from a cesium vapor cell. Phase modulation of the excitation laser is used to directly reference this scale to a rubidium frequency standard. To confirm the frequency scale accuracy, we also measure the magnetic dipole and electric quadrupole hyperfine coupling constants:  $A = 16.36(15)$  MHz and  $B = -0.7(8)$  MHz. These hyperfine coupling constants agree with previous measurements [18, 19].

## Acknowledgments

The work of M.S.S. was supported in part by National Science Foundation Grant No. PHY-07-58088. The work of A.K., C.T., and J.G. were supported in part by the National Science Foundation Grant No. PHY-06-53107. We express our sincere gratitude to Richard Mertz, Physics Department Technician at Lafayette College, for his assistance in fabricating the experimental apparatus.

- 
- [1] J. Mitroy, M. S. Safronova, and C. W. Clark, J. Phys. B **43**, 202001 (2010).  
 [2] M. S. Safronova, D. Jiang, B. Arora, C. W. Clark, M. G. Kozlov, U. I. Safronova, and W. R. Johnson, IEEE Trans.

- Ultrason. Ferroelectrics and Frequency Control **57**, 94 (2010).  
 [3] B. Arora, M. S. Safronova, and C. W. Clark, Phys. Rev. A **76**, 052516 (2007).

- [4] C. Wood, S. Bennett, D. Cho, B. Masterson, J. Roberts, C. Tanner, and C. Wieman, *Science* **275**, 1759 (1997).
- [5] S. C. Bennett and C. E. Wieman, *Phys. Rev. Lett.* **82**, 2484 (1999).
- [6] J. M. Amini and H. Gould, *Phys. Rev. Lett.* **91**, 153001 (2003).
- [7] L. R. Hunter, D. Krause, K. E. Miller, D. J. Berkeland, and M. B. Boshier, *Opt. Comm.* **94**, 210 (1992).
- [8] L. R. Hunter, D. Krause, S. Murthy, and T. W. Sung, *Phys. Rev. A* **37**, 3283 (1988).
- [9] C. E. Tanner and C. Wieman, *Phys. Rev. A* **38**, 162 (1988).
- [10] W. A. van Wijngaarden and J. Li, *J. Quant. Spect. Rad. Transf.* **52**, 555 (1994).
- [11] E. Iskrenova-Tchoukova, M. S. Safronova, and U. I. Safronova, *J. Comput. Meth. Sci. Eng.* **7**, 521 (2007).
- [12] M. Auzinsh, K. Bluss, R. Ferber, F. Gahbauer, A. Jarmola, M. S. Safronova, U. I. Safronova, and M. Tamanis, *Phys. Rev. A* **75**, 022502 (2007).
- [13] M. S. Safronova and U. I. Safronova, *Phys. Rev. A* **83**, 012503 (2011).
- [14] D. Jiang, B. Arora, M. S. Safronova, and C. W. Clark, *J. Phys. B* **42**, 154020 (2009).
- [15] B. Arora, M. S. Safronova, and C. W. Clark, *Phys. Rev. A* **76**, 052509 (2007).
- [16] R. Schmeider, *Am. J. Phys.* **40**, 297 (1972).
- [17] A. Kortyna, V. Fiore, and J. Farrar, *Phys. Rev. A* **77**, 062505 (2008).
- [18] A. Kortyna, N. A. Masluk, and T. Bragdon, *Phys. Rev. A* **74**, 022503 (2006).
- [19] C. Tai, W. Happer, and R. Gupta, *Phys. Rev. A* **12**, 736 (1975).
- [20] I. S. Lim, J. K. Laerdahl, and P. Schwerdtfeger, *J. Chem. Phys.* **116**, 172 (2002).
- [21] W. R. Johnson, S. A. Blundell, and J. Sapirstein, *Phys. Rev. A* **37**, 307 (1988).
- [22] M. S. Safronova and W. R. Johnson, *Adv. At. Mol., Opt. Phys.* **55**, 191 (2007).
- [23] C. E. Moore, *Atomic Energy Levels (Molybdenum-Actinium NSRDS-NBS 35)*, vol. 3 (US GPO, Washington DC, 1971).
- [24] Yu. Ralchenko, F.-C. Jou, D.E. Kelleher, A.E. Kramida, A. Musgrove, J. Reader, W.L. Wiese, and K. Olsen (2005). NIST Atomic Spectra Database (version 3.0.2), [Online]. Available: <http://physics.nist.gov/asd3> [2006, January 4]. National Institute of Standards and Technology, Gaithersburg, MD.